Check for updates

Full optical confinement in 1D mesoscopic photonic crystal-based microcavities: an experimental demonstration

A. MONMAYRANT,[1] M. GRANDE,[2] B. FERRARA,[2] G. CALÒ,[2] O. GAUTHIER-LAFAYE,[1] A. D'ORAZIO,[2] B. DAGENS,[3] V. PETRUZZELLI,[2] AND G. MAGNO[3,*]

[1]LAAS-CNRS, Université de Toulouse, CNRS, INSA, UPS, Toulouse, France
[2]Dipartimento di Ingegneria Elettrica e dell'Informazione (DEI), Politecnico di Bari, Via Re David 200, 70125, Italy
[3]Centre de Nanosciences et de Nanotechnologies, CNRS, Université Paris-Sud, Université Paris-Saclay, C2N-Orsay, 91405 Orsay Cedex, France
*giovanni.magno@c2n.upsaclay.fr

Abstract: Full light confinement in mesoscopic photonic crystal membranes, forming a mesoscopic self-collimating 1D Fabry-Pérot cavity, was predicted by Magno et al. [Opt. Lett. 39(14), 4223-4226 (2014)], using 2D calculations. Mesoscopic self-collimating cavities enable full light confinement despite the lack of index- or bandgap-guiding along one direction due to the flatness of the cavity reflectors. In this paper, we study these cavities using 3D-FDTD modelling and demonstrate that 3D light confinement survives the high losses inherent to the out-of-plane diffraction. Furthermore, we report an experimental demonstration at telecom wavelength on GaAs membranes with Q factors above 1700. This structure may pave the way for the fabrication of innovative configurations devoted to biochemical sensing and optical tweezing for nanoparticle manipulation thanks to its translational invariance property.

References and links

1. H. Kosaka, T. Kawashima, A. Tomita, M. Notomi, T. Tamamura, T. Sato, and S. Kawakami, "Self-collimating phenomena in photonic crystals," Appl. Phys. Lett. **74**(9), 1212–1214 (1999).
2. J. Arlandis, E. Centeno, R. Pollès, A. Moreau, J. Campos, O. Gauthier-Lafaye, and A. Monmayrant, "Mesoscopic self-collimation and slow light in all-positive index layered photonic crystals," Phys. Rev. Lett. **108**(3), 037401 (2012).
3. G. Magno, M. Grande, A. Monmayrant, F. Lozes-Dupuy, O. Gauthier-Lafaye, G. Calò, and V. Petruzzelli, "Controlled reflectivities in self-collimating mesoscopic photonic crystal," J. Opt. Soc. Am. B **31**(2), 355–359 (2014).
4. G. Magno, A. Monmayrant, M. Grande, F. Lozes-Dupuy, O. Gauthier-Lafaye, G. Calò, and V. Petruzzelli, "Stable planar mesoscopic photonic crystal cavities," Opt. Lett. **39**(14), 4223–4226 (2014).
5. G. Magno, A. Monmayrant, M. Grande, F. Lozes-Dupuy, O. Gauthier-Lafaye, G. Calò, and V. Petruzzelli, "Stable planar microcavities based on mesoscopic photonic crystals," Proc. SPIE **8988**, 89881G (2014).
6. G. Magno, *et al.*, "Self-collimation in mesoscopic photonic crystals: from reflectivity management to stable planar cavities," in *2014 16th International Conference on Transparent Optical Networks* (ICTON) (IEEE, 2014), pp. 1–4.
7. J. Arlandis, Étude de la mise en forme spatio-temporelle de la lumière dans les cristaux photoniques et les métamatériaux (Université Blaise Pascal U.F.R. Sciences et Technologies), 2012.
8. G. Magno, A. Monmayrant, M. Grande, O. Gauthier-Lafaye, G. Calò, B. Dagens, and V. Petruzzelli, "Full optical confinement in 1D Mesoscopic Photonic Crystal-based microcavities: A preliminary experimental demonstration," in *International Conference on Transparent Optical Networks* (2016), p. 7550433.
9. B. Ferrara, M. Grande, G. Calò, A. D'Orazio, B. Dagens, A. Monmayrant, O. Gauthier-Lafaye, V. Petruzzelli, and G. Magno, "Optical sensor based on a mesoscopic photonic crystal microcavity," in *ACP2016-Asia Communications and Photonics Conference*, OSA Technical Digest (2016).
10. are A. Larrue, O. Bouchard, A. Monmayrant, O. Gauthier-Lafaye, S. Bonnefont, A. Arnoult, P. Dubreuil, and F. Lozes-Dupuy, "Precise Frequency Spacing in Photonic Crystal DFB Laser Arrays," IEEE Photonics Technol. Lett. **20**(24), 2120–2122 (2008).

1. Introduction

Mesoscopic Photonic Crystals (MPhCs) support the Mesoscopic Self-Collimation (MSC) phenomenon, which ensures 'guideless' waveguiding in linear media. As in traditional Self-Collimation (SC) [1], this behaviour can be reached by engineering the angular anisotropy [2] of the crystal. This is a change of paradigm as light guiding occurs without any need for alignment with a guiding structure. In fact, a MPhC is a 1D-periodic superstructure that can be fabricated by cascading slabs of different materials (or metamaterials) exhibiting opposite spatial dispersion, such as slab of PhCs in the self-focussing regime and slabs of bulk materials. From the spatial dispersion engineering point of view, for a specific direction, MSC is obtained when the focusing properties of the PhC slabs compensate the natural defocusing of the bulk material slabs [2–9]. This 'guideless' waveguiding paves the way for the conception of structures showing lateral translational invariance. A key advantage of MSC as compared to SC, is that several optical properties can be achieved simultaneously, thanks to higher degrees of freedom: input facet impedance perfect matching [3], stable Fabry-Pérot-like microcavities having flat parallel mirrors with an improved reflectivity able to reflect even non-paraxial beams, as curved mirrors do [4, 5], slow light waveguides [2, 7] compensation of time and space dispersion to achieve linear solitons [7].

One original application of MPhCs is the design of high sensitivity and high Q-factor microcavities [4–6,8,9] on thin membranes. However, these theoretical predictions are based on 2D calculations that ignore vertical losses due to out-of-plane diffraction. As MSC occurs well above the light line (due to large meso-period as compared to the wavelength), these losses are potentially high and might be detrimental to the predicted high-Q confinement.

In this paper, we report on 3D-FDTD simulations and experimental demonstration of a fabricated MPhC Fabry-Pérot microcavity exhibiting high-Q, 3D-light confinement.

2. 3D modelling

Figure 1 depicts a sketch of the MPhC microcavity numerically investigated with 3D-FDTD (Lumerical FDTD Solutions), comprised of two MPhC mirrors (MM) on each side of a homogeneous defect. The geometry of the microcavity is based on the 2D numerical analysis reported in [4]. Each MM is obtained by interleaving focusing slabs, constituted by 13 rows of holes of a 45°-tilted square-lattice PhC (with lattice constant $a = 350$ nm, hole radius $r = 0.25 \times a = 87.5$ nm and an overall width $d_c = 9.192 \times a$), and defocusing slabs, constituted by bulk material with a refractive index n_b and a width $d_b = 2.612 \times a$ (a sketch of the MPhC unitary cell is shown in Fig. 1(b)). The cavity defect width is $W = 5.32 \times a$. We modelled the device by considering a 276-nm-thick GaAs membrane ($n_b = 3.31$ at 1550 nm), fully surrounded by air having refractive index $n = 1$.
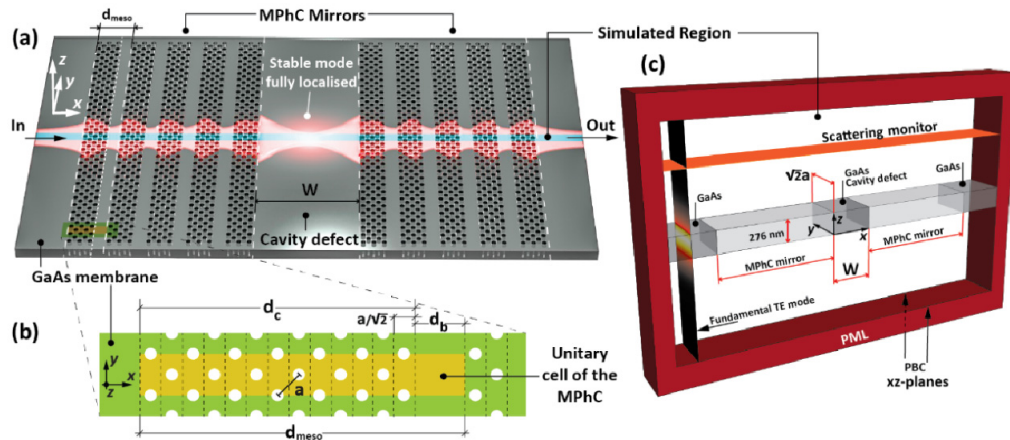
Fig. 1. (a) Sketch of the fabricated MPhC microcavity. The highlighted green and yellow area is reported in (b), where the yellow one represents the elementary cell of the MPhC. The highlighted light blue strip represents the portion of the structure that is actually calculated in the 3D-FDTD simulation. (b) Sketch of the MPhC elementary cell. (c) Sketch of the FDTD calculation region. The red region bordering the cell along the *x*- and *z*-directions represent the PML boundary conditions. The two black vertical arrows indicate the *xz*-planes where the PBCs enclose the computational region along the y-direction. The orange strip, parallel to the *xy*-plane, represents the monitor where collect the scattered power is collected.

Since the structure is periodic along the y-direction, showing a period $\sqrt{2} \times a$ (see Fig. 1(c)), we have imposed periodic boundary conditions (PBCs) to the computational cell boundaries perpendicular to this direction. PMLs are imposed at the boundaries perpendicular to the remaining directions (*x*- and *z*-directions). The structure is excited in by injecting a broadband source (1460 *nm* < λ < 1580 *nm*) having a spatial distribution matching that of the fundamental TE mode (with the *x*-component of the electric field $E_x = 0$) of the membrane (at λ = 1520 *nm*).

Figure 2 shows the simulated spectrum of the vertically scattered light above the cavity. In good agreement with 2D-FDTD simulations reported in [4], despite the vertical losses, a long-lived mode showing a high-Q spectral peak around 1480 *nm* is observed with a Q-factor of about 4773 (≈half of the corresponding 2D one). Another weaker peak, with a lower Q factor is also observed around 1551 *nm* (Q-factor equal to about 889) and which was observed in [4].
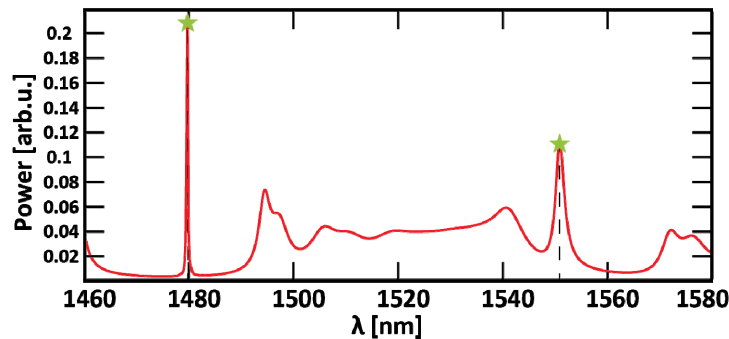

Fig. 2. FDTD vertically scattered light spectrum (normalized to the input power). The two peaks suggesting the formation of an optical mode inside the cavities are highlighted by two markers: one at 1480 nm and one at 1551 nm.

In order to investigate the nature of both the modes, a second set of 3D-FDTD simulations were carried out where the total electric field and the *z*-component of the Poynting vector were recorded. Results are shown on Fig. 3: total electric field at 1480 *nm* (a) and at 1551 *nm* (b) and *z*-component of the Poynting vector at 1480 *nm* (c) and 1551 *nm* (d). To highlight the vertically scattered light above the cavity, self-normalized Poynting vector depicted in Figs. 3(c) and 3(d) is plotted using a logarithmic scale.
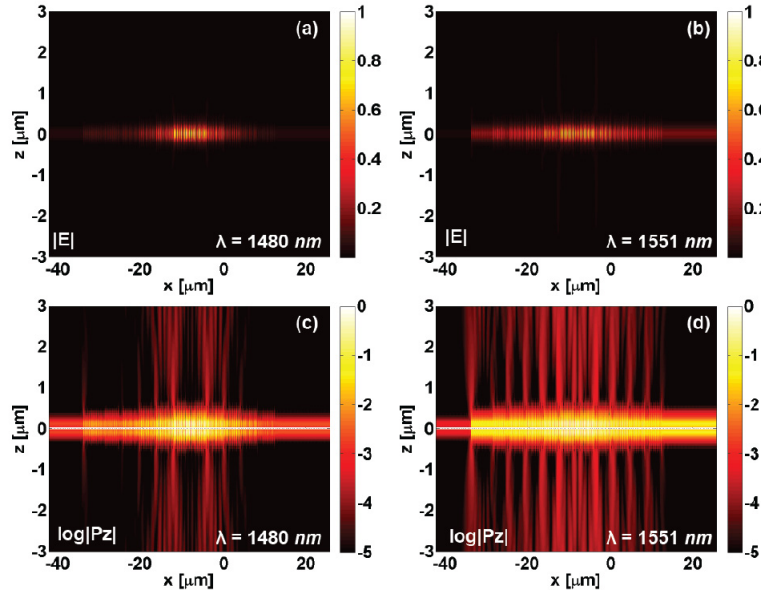

Fig. 3. Self-normalised magnitude of the total electric field (a-b) and (c-d) z-component of the logarithm of the self-normalised Poynting vector at 1480 nm and 1551 nm, respectively.

From these simulations, we conclude that both the spectral peaks correspond to modes that are fully localized: in *xy*-plane (2D) by the MSC cavity, and in the vertical direction by the membrane with partial leaking out of the membrane.

3. Sample fabrication and characterization

Several samples with the geometry described in Fig. 1 were fabricated on suspended GaAs membranes in a three-step process described in [10]. Firstly, e-beam lithography was used to define the pattern in an electronic resist and form a mask that, in a second step, was used to etch the PhC holes using dry etching (ICP - RIE). In a last step, the samples were immersed into a hydrofluoric acid bath to remove a 1.5μm-thick AlGaAs sacrificial layer.

Figures 4(a) and 4(b) shows a scanning electron microscope (SEM) in-plane image of the micro-cavity (with an overall length along *x* and *y* of 41.3 μm and 92.5 μm, respectively).

Figure 4(c) shows the optical characterization set-up of the sample: the beam of a tunable laser (spanning 1460 – 1580 *nm*) is focused on the sample facet using two aspherical lenses; a polarizer, placed in between the two lenses, controls the input light polarization. A microscope system, composed by a microscope objective and a VIS-IR vidicon camera, collects the scattered light and displays it on a monitor. Finally, the video signal is acquired by a commercial acquisition card and numerically processed.

An image of the scattered light is acquired for each wavelength, forming an hyperspectral cube $A(p_x,p_y,\lambda_p)$, where λ_p is a given wavelength, p_x and p_y are the pixel indices along the *x* and *y* directions, respectively.

In Fig. 4(a) the alignment position of the first and last row of the matrix of pixels ($p_x = 1$ and $p_x = p_{x,cav}$ corresponding to the beginning and end of the cavity, respectively) are superimposed on the SEM image.
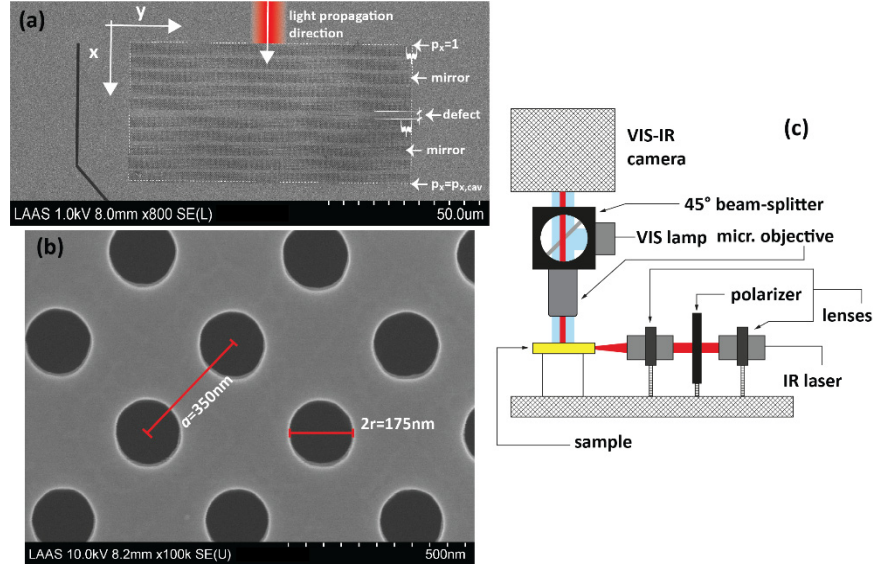

Fig. 4. (a) In-plane SEM image of a fabricated MPhC based microcavity having a lattice constant $a = 350$ nm and a hole radius $r = 0.25 \times a = 87.5$ nm. The white arrows on the right indicate the position of the beginning and the end of the cavity and the defect position. The red stripe with a superimposed white arrow indicates the incident light direction. (b) Close-up of (a) inside a PhC slab. (c) Sketch of the optical characterization set-up of the sample.

In order to calculate the experimental vertically scattered light, we define a pseudospectral map $M(p_x,\lambda_p)$ as the sum of the pixel intensities A along the transverse direction of the cavity (y-direction):

$$M\left(p_x,\lambda_p\right)=\sum_{p_y}A\left(p_x,p_y,\lambda_p\right). \tag{2}$$

The pseudospectral map M(p_x,λ_p) allows to determine the following quantities:

$$S\left(\lambda_p\right)=\sum_{p_x=1}^{p_{x,cav}}M\left(p_x,\lambda_p\right) \tag{3a}$$

$$N\left(\lambda_p\right)=\sum_{p_x=p_{x,cav}+1}^{p_{x,end}}M\left(p_x,\lambda_p\right) \tag{3b}$$

$$\alpha=\frac{p_{x,cav}-1}{p_{x,end}-\left(p_{x,cav}+1\right)} \tag{3c}$$

The useful signal is represented by $S(\lambda_p)$ that is the pseudospectral map integrated along the x-direction inside the cavity; the noise is represented by $N(\lambda_p)$ that is the pseudospectral map integrated along the x-direction outside of the cavity; α is a corrective coefficient that normalizes the cavity length with respect to the length of the noise region. Finally, the pseudospectrum $I(\lambda_p)$ is obtained as follows:

$$I\left(\lambda_p\right)=S\left(\lambda_p\right)-\alpha\cdot N\left(\lambda_p\right) \tag{4}$$

Figure 5(a) shows the experimental pseudospectral map of the fabricated microcavity in the wavelength range of interest. The final experimental vertically scattered light spectrum is evaluated by integrating the map along the *x*-axis.

Figure 5(b) shows the final experimental pseudospectrum (blue curve) that is compared with the simulated normalized vertically scattered light spectrum calculated previously (red curve). This simulated spectrum is normalized to its maximum (as the pseudospectrum). The experimental results show a good agreement with the numerical ones. Specifically, in the experimental pseudospectrum the resonant peaks within the bandgaps, corresponding to the formation of a stable cavity mode, are at $\lambda_0 = 1482.2$ nm (green square mark) and $\lambda_3 = 1547$ *nm* (green star mark) allowing for a *Q* factor equal to 1720 and 1170, respectively. The differences between simulated and measured Q factors are attributed to the fact that the experimental beam is laterally confined, while in the simulation, an infinitely large beam was used.

To experimentally investigate the localization of the mode, we concentrate on the $\lambda_3 = 1547$ *nm* mode. We choose this mode as it exhibits a higher signal to noise ratio on the camera signal as compared to the $\lambda_0 = 1482.2$ *nm* mode. Figure 6 depicts the collected scattered light images at $\lambda_1 = 1545$ *nm*, $\lambda_2 = 1546$ *nm*, $\lambda_3 = 1547$ *nm* and $\lambda_4 = 1548$ *nm*. In particular, Fig. 6(c) illustrates the formation of a stable mode at λ_3. At the same time, the region beyond the output facet in Fig. 6(c) is dark due to absence of scatterers (PhC holes and PhC/bulk interfaces).
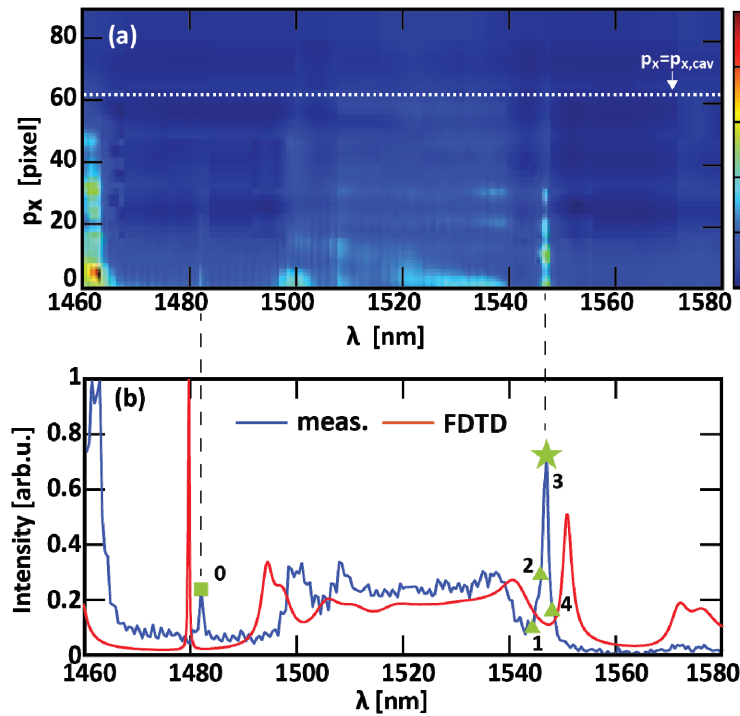

Fig. 5. (a) Measured pseudospectral map of the fabricated microcavity with *a* = 350 nm. The superimposed horizontal white dotted line indicates the pixel labelled $p_{x,cav}$. (b) Experimental pseudospectrum (blue curve) and the simulated self-normalized scattering spectrum (red curve), which corresponds to the result shown on Fig. 2. The green squared mark and the green star mark indicate the resonant peaks wavelengths $\lambda_0 = 1482.2$ *nm* and $\lambda_3 = 1547$ *nm*, respectively. The green triangle marks denote the wavelengths $\lambda_1 = 1545$ *nm*, $\lambda_2 = 1546$ *nm* and $\lambda_4 = 1548$ *nm*, corresponding to the subfigures shown in Fig. 6.
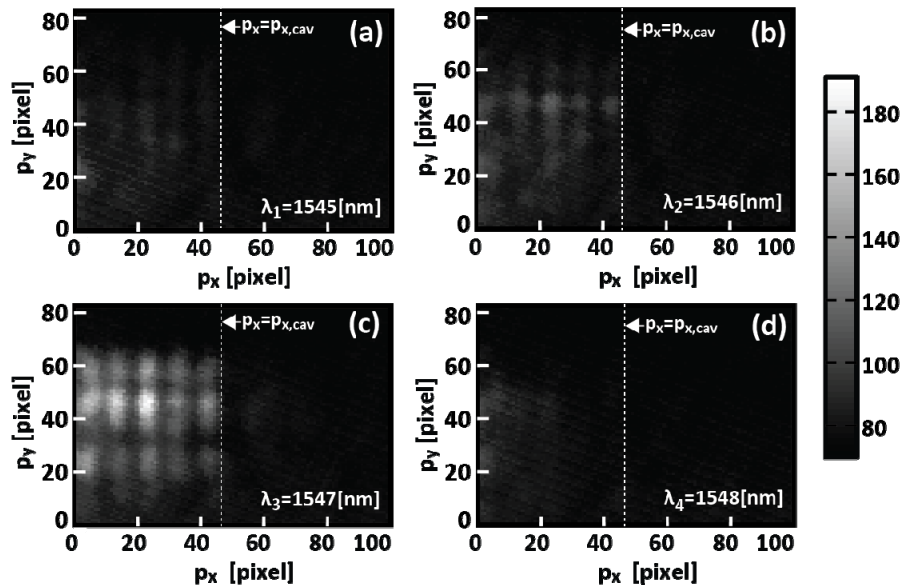
Fig. 6. Collected scattered light at wavelengths (a) λ_1, (b) λ_2, (c) λ_3 and (d) λ_4. The p_y-axis and the superimposed white dotted line indicate the input facet ($p_x = 1$) and the output facet ($p_x = p_{x,cav}$) of the cavity, respectively.

4. Conclusion

In conclusion, we demonstrated experimentally that MPhC microcavities can confine light in 3D using a Fabry-Pérot-like 2D cavity on a slab. Despite being well above the light cone and thus being well coupled to the vertical axis, the confined mode exhibits experimental Q factor in excess of 1700. These experimental results are in agreement with the 3D numerical findings in terms of resonant wavelength and Q-factors.

These results pave the way for a new class of devices showing translational invariance and strong near-field localization, together with a strong coupling with surroundings. Those features could be extremely valuable for optical devices devoted to biochemical sensing, optical tweezing and nanoparticle manipulation and for the design of innovative tweeze-and-sense micro- and nano-object systems that could be integrated in microfluidic systems and labs-on-chip.